Symposium on Materials Science

Mátraháza, Hungary, October 4-6, 2021

Editor:
Miklós Fried
Institute of Microelectronics and Technology, Óbuda University
2022

Organizing and Programme Committee:

Miklós Fried (editor, Institute of Microelectronics and Technology, Óbuda University)

Ákos Nemcsics (Institute of Microelectronics and Technology, Óbuda University)

Attila Bonyár (Department of Materials Science and Engineering, Budapest University of Technology and Economics)

Péter Petrik (Institute of Technical Physics and Material Science, Centre for Energy Research)

András Deák (Institute of Technical Physics and Material Science, Centre for Energy Research)

ISBN 978-963-449-290-0

Table of contents

Dániel Péter Szekrényes, Dániel Zámbó, Zsolt Zolnai, Rita Némedi, Norbert Nagy and András Deák: *Investigating the electric double layer directed self assembly of oppositely charged gold nanospheres* 7

Zoltán Farkas, Antal Ürmös and Ákos Nemcsics: *Soft-computing based Technological Support for Droplet Epitaxially Grown Zero-dimensional GaAs Structures* 11

Benjamin Kalas, György Sáfrán, Miklós Serényi, Kárpát Ferencz, Miklós Fried, and Péter Petrik: *Surface-enhanced Kretschmann-Raether ellipsometry based on plasmonic, Bragg and waveguide structures* 12

Dániel Zámbó: *Nanoparticle gel networks as a novel platform in electrochemical sensing* 15

József Bálint Renkó, Alekszej Romanenko, Péter János Szabó, Péter Petrik, Attila Bonyár: *Analysis of the microstructure of color etched low carbon steel with spectroscopic ellipsometry* 20

A. Romanenko, E. Agócs, Z. Hózer, P. Petrik and M. Serényi: *In-situ ellipsometry on the oxidation of zirconium at medium temperatures* 25

D. Olasz., V. Kis, P. Petrik, B. Kalas, G. Sáfrán: *Microstructure of composition spread YTiO thin films* 29

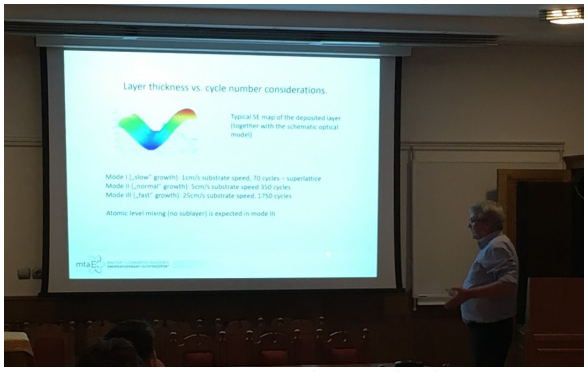

Lecturers: Zoltán Lábadi

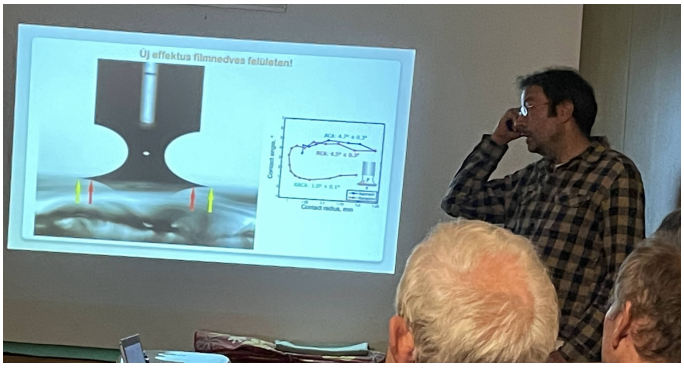

Norbert Nagy

Lecturers: Dániel Péter Szekrényes

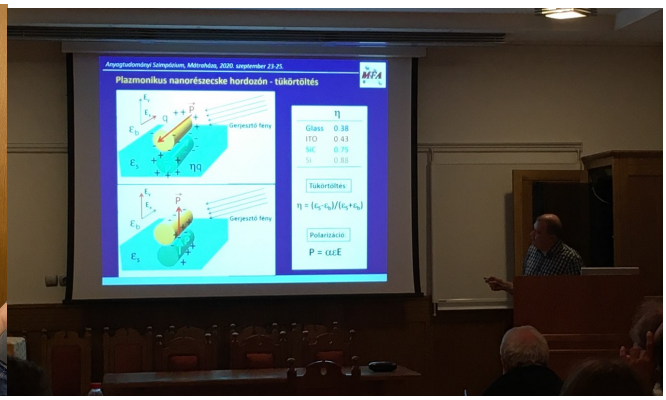

Zsolt Zolnai

Lecturers: Ákos Nemcsics

György Sáfrán

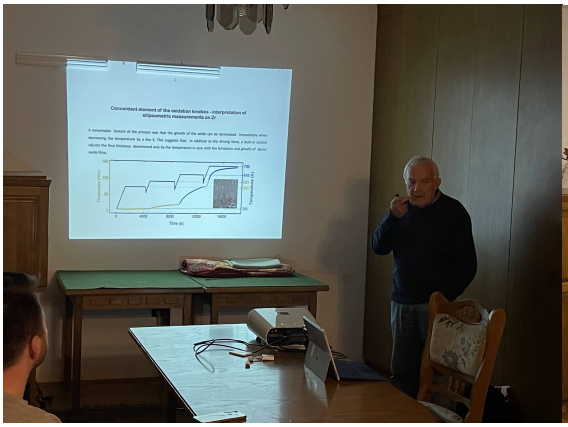

Lecturers: Miklós Serényi Miklós Fried

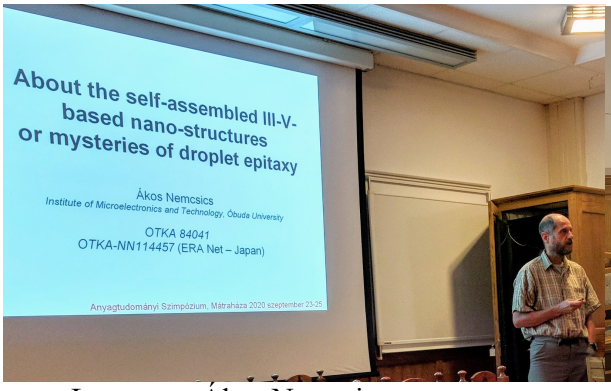

Lecturers: Ákos Nemcsics András Deák

Lecturers: Dániel Zámbó Péter Petrik

Lecturers: Benjamin Kalas Alekszej Romanenko

Lecturers: József Bálint Renkó Attila Bonyár

The Symposium

Investigating the electric double layer directed self-assembly of oppositely charged gold nanospheres

Dániel Péter Szekrényes[1*], Dániel Zámbó[1], Zsolt Zolnai[1], Rita Némedi[1], Norbert Nagy[1] and András Deák[1]

[1]*Institute of Technical Physics and Material Science, Centre for Energy Research, Budapest, H-1121 Hungary*

Tailoring the colloidal interactions around nanoparticles by controlling the composition of their surface layer enables the rational design of particle superstructures in self-assembly procedures. In the present work, gold nanoparticles modified by oppositely charged thiol ligands are prepared to create sphere-sphere oligomers via electric double layer interaction directed self-assembly process. On the basis of colloidal interaction calculations and optical experiments performed both at bulk and single particle level, it has been shown that the size and the surface charge of the particles and the chain length of the capping ligands have a profound impact on the structure of the developed particle assemblies.

Keywords: gold nanoparticles, self-assembly, plasmonics, single particle spectroscopy, colloidal interactions

Introduction

Over the past few decades, numerous investigations have been carried out concerning the controlled formation of nanoparticle assemblies. Strategies elaborated in these studies typically rely on tuning and balancing the attractive and repulsive colloidal interactions between the particles such as dispersion,[1,2] electric double layer (EDL)[3–5] or steric interactions.[6,7] Using noble metal nanoparticles as a model system provides the possibility to monitor the formation of particle assemblies since their optical response heavily depends on the geometry of the given structure (size and shape of consisting particles, interparticle distance, relative geometrical arrangement etc.) owing to plasmon coupling between the particles.[6,8,9] In this work, we investigated the EDL directed self-assembly of oppositely charged gold nanospheres and how the size of the particles and the chain length of different capping ligands influence on the colloidal interactions, determining the structure, thus the optical response of the particle assemblies. In order to get a better insight into the self-assembly process, not only bulk optical spectroscopy experiments were carried out, but also single particle techniques, such as scanning electron microscopy (SEM) and dark field scattering spectroscopy, were utilised to characterise the resulting particle oligomers on solid substrate (Figure 1.b).

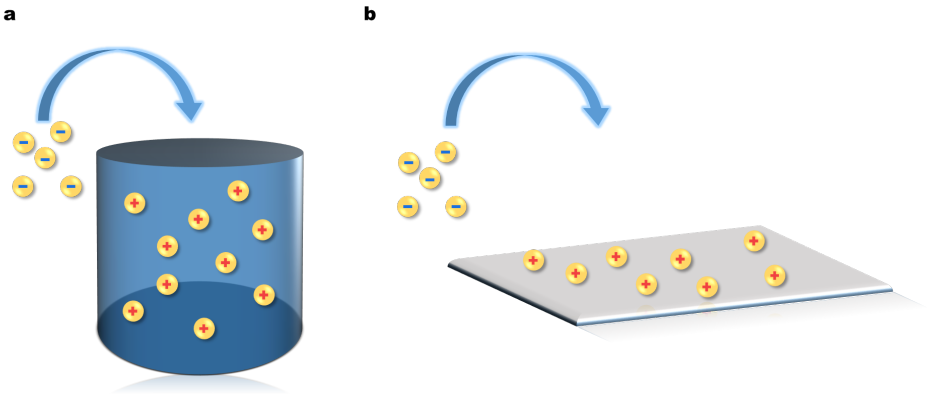

Figure 1. Concept of EDL directed self-assembly experiments when the process is carried out in (a) liquid phase and (b) in solid-liquid interface.

Experimental section

Gold nanospheres stabilised by either CTA^+ or citrate were prepared based on previously published synthesis protocols.[10–13] The surface modification of these particles was performed using thiol ligands with different size and charge state to tailor colloidal interactions. The ligand exchange was monitored by visible spectrometry, dynamic light scattering and electrophoretic mobility measurements. The self-assembly of

oppositely charged gold nanospheres was performed by adding increasing amount of the solution of negatively charged particles (covered by citrate, MUA or carboxylated PEG) to the solution of MTA^+-capped nanospheres and the process was monitored by visible spectrometry (Figure 1.a). As reference sample, gold nanospheres capped by the neutral 5 kDa PEG was used. The 48 nm MTA^+-stabilised particles were mixed with either 45 nm or 15 nm negatively charged nanospheres. To obtain more information on the structure of particle assemblies, sphere-sphere heterooligomers were created on a silicon substrate by immersing the immobilised MTA^+-capped particles in the sol of negatively charged gold nanospheres (Figure 1.b). The scattering spectra of solid supported individual particle oligomers were acquired and the actual structure of the given particle assemblies was obtained via correlative scanning electron microscopy, that is exactly the same object were investigated by spectroscopy and SEM. The colloidal interactions were calculated considering van der Waals, EDL and steric interactions.[14–16]

Results

According to the results of Bishop et al.[17], differently charged particles, which are mixed in a solution, precipitate only at the point of nanoparticle electroneutrality, that is, when the charges on the particles are compensated and the net charge is zero. Based on this effect, the positively charged MTA^+-covered nanoparticles were titrated by an increasing fraction of negatively charged thiol-capped nanospheres.

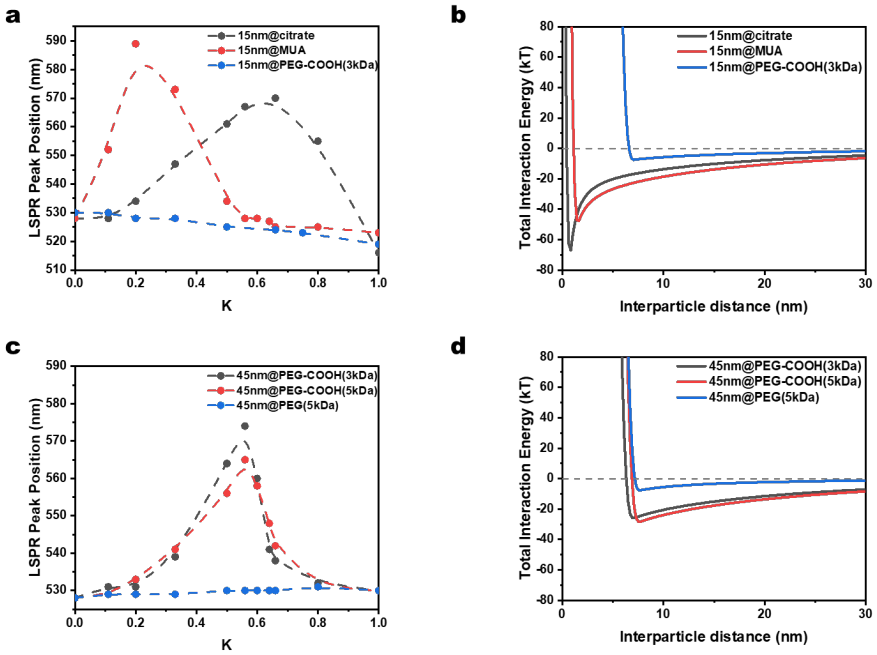

Figure 2. Plasmon resonance peak shift upon increasing the amount of negatively charged particles when the negatively charged particles are (a) significantly smaller (15 nm) and when (c) have ca. the same size (45 nm) relative to the dimension of MTA^+-capped spheres (48 nm). K means the fraction of negatively charged particles relative to MTA^+-covered spheres. (b)(d) Calculated total interaction energy for the corresponding particle systems.

Figure 2.a shows the localised surface plasmon resonance (LSPR) redshift for the mixed nanoparticle system as a function of the fraction of negatively charged 15 nm particles relative to the amount of 48 nm MTA^+-capped spheres (*K*). The addition of citrate or MUA-covered particles induce a noticeable redshift, indicating the EDL directed aggregation of the samples. However, when carboxylated PEG was used as a negatively charged capping agent there is no such a pronounced plasmon interaction, that is, no redshift significant can be observed. When the size of negatively charged particles was changed to 45 nm, the addition of carboxylated PEG-capped particles leads to a redshift in the bulk optical spectrum around *K*=0.5. as shown in Figure 2.c Neutral PEG-chains, however, can stabilise the system, since no considerable shift can be seen in the bulk optical spectrum. Colloidal interaction calculations (Figure 2.b and d.) show that the decreasing size of thiol ligands on the particle surface results in deeper potential well in total interaction energy and shorter interparticle distance due to reduced repulsive steric interaction. In addition, the increase of the size of the particles results in higher attractive dispersion interaction, facilitating the EDL directed self-assembly of the nanoparticle system. These observations agree well with the experimental results.

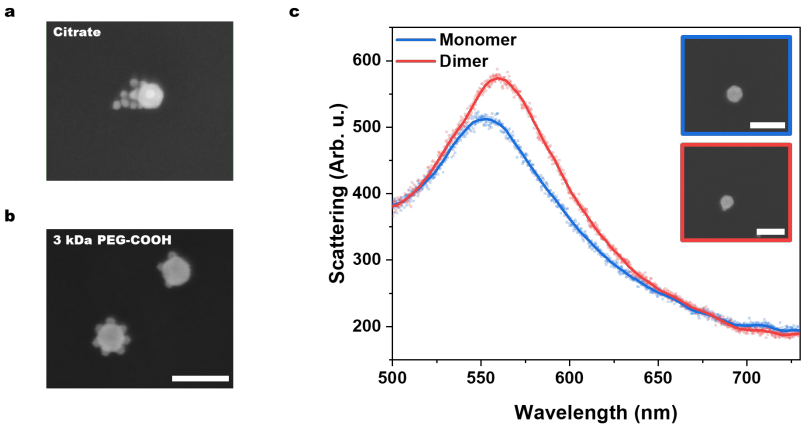

Figure 3. The representative SEM images of heterooligomers when the negatively charged spheres were covered by (a) citrate and (b) 3 kDa carboxylated PEG. (c) Single particle scattering spectra of individual gold nanosphere (blue) and sphere-sphere heterodimer (red). The inset shows the SEM micrographs of the corresponding nanoobjects. Scale bar is 100 nm.

To obtain more direct information on the structure of developed particle assemblies, single particle spectroscopy correlated with SEM were performed on particle heterooligomers developed by immersing immobilised 48 nm MTAB-covered nanospheres in the sol of 14 nm citrate or 3 kDa PEG-COOH-capped particles. In the former case, large particle assemblies evolved (Figure 3.a), making the interpretation of their optical response cumbersome. By using PEG-COOH covered particles, however, smaller oligomers evolved (Figure 3.b), which make them ideal candidates for single particle optical investigations. The absence of large aggregates is consistent with colloidal interaction calculations and ensemble spectroscopy results. In Figure 3.c, the scattering spectra of a monomer and a dimer can be seen. As expected, the heterodimer shows a significant redshift, peak broadening and an intensity increase relative to the optical spectrum of the monomer due to plasmon coupling. These results are promising and suggest that fine-tuning the particle size and PEG chain length should enable the controlled preparation of few-particle assemblies.

Acknowledgement

The authors acknowledge the funding of the National Research, Development and Innovation Office (NKFIH FK-128327, KH-129 578). D.P.Sz is grateful for the support of the József Varga and Pro Progression Foundations.

References

(1) Sau, T. K.; Murphy, C. J. Self-Assembly Patterns Formed upon Solvent Evaporation of Aqueous Cetyltrimethylammonium Bromide-Coated Gold Nanoparticles of Various Shapes. *Langmuir* **2005**, *21* (7), 2923–2929. https://doi.org/10.1021/la047488s.
(2) Jana, N. R. Shape Effect in Nanoparticle Self-Assembly. *Angew. Chem. Int. Ed.* **2004**, *43* (12), 1536–1540. https://doi.org/10.1002/anie.200352260.
(3) Pothorszky, Sz.; Zámbó, D.; Deák, T.; Deák, A. Assembling Patchy Nanorods with Spheres: Limitations Imposed by Colloidal Interactions. *Nanoscale* **2016**, *8* (6), 3523–3529. https://doi.org/10.1039/C5NR08014B.
(4) Pothorszky, S.; Zámbó, D.; Szekrényes, D.; Hajnal, Z.; Deák, A. Detecting Patchy Nanoparticle Assembly at the Single-Particle Level. *Nanoscale* **2017**, *9* (29), 10344–10349. https://doi.org/10.1039/C7NR02623D.
(5) Szekrényes, D. P.; Pothorszky, S.; Zámbó, D.; Deák, A. Detecting Spatial Rearrangement of Individual Gold Nanoparticle Heterodimers. *Phys. Chem. Chem. Phys.* **2019**, *21* (19), 10146–10151. https://doi.org/10.1039/C9CP01541H.
(6) Zámbó, D.; Radnóczi, G. Z.; Deák, A. Preparation of Compact Nanoparticle Clusters from Polyethylene Glycol-Coated Gold Nanoparticles by Fine-Tuning Colloidal Interactions. *Langmuir* **2015**, *31* (9), 2662–2668. https://doi.org/10.1021/la504600j.
(7) Zámbó, D.; Pothorszky, Sz.; Brougham, D. F.; Deák, A. Aggregation Kinetics and Cluster Structure of Amino-PEG Covered Gold Nanoparticles. *RSC Adv.* **2016**, *6* (32), 27151–27157. https://doi.org/10.1039/C6RA03902B.
(8) Shao, L.; Fang, C.; Chen, H.; Man, Y. C.; Wang, J.; Lin, H.-Q. Distinct Plasmonic Manifestation on Gold Nanorods Induced by the Spatial Perturbation of Small Gold Nanospheres. *Nano Lett.* **2012**, *12* (3), 1424–1430. https://doi.org/10.1021/nl2041063.
(9) Shao, L.; Woo, K. C.; Chen, H.; Jin, Z.; Wang, J.; Lin, H.-Q. Angle- and Energy-Resolved Plasmon Coupling in Gold Nanorod Dimers. **2010**, *4* (6), 10.
(10) Pazos-Perez, N.; Garcia de Abajo, F. J.; Fery, A.; Alvarez-Puebla, R. A. From Nano to Micro: Synthesis and Optical Properties of Homogeneous Spheroidal Gold Particles and Their Superlattices. *Langmuir* **2012**, *28* (24), 8909–8914. https://doi.org/10.1021/la3002898.
(11) Xia, H.; Xiahou, Y.; Zhang, P.; Ding, W.; Wang, D. Revitalizing the Frens Method To Synthesize Uniform, Quasi-Spherical Gold Nanoparticles with Deliberately Regulated Sizes from 2 to 330 Nm. *Langmuir* **2016**, *32* (23), 5870–5880. https://doi.org/10.1021/acs.langmuir.6b01312.
(12) Turkevich, J.; Stevenson, P. C.; Hillier, J. A Study of the Nucleation and Growth Processes in the Synthesis of Colloidal Gold. *Discuss. Faraday Soc.* **1951**, *11*, 55. https://doi.org/10.1039/df9511100055.
(13) Ziegler, C.; Eychmüller, A. Seeded Growth Synthesis of Uniform Gold Nanoparticles with Diameters of 15−300 Nm. *J. Phys. Chem. C* **2011**, *115* (11), 4502–4506. https://doi.org/10.1021/jp1106982.
(14) Kleshchanok, D.; Lang, P. R. Steric Repulsion by Adsorbed Polymer Layers Studied with Total Internal Reflection Microscopy. *Langmuir* **2007**, *23* (8), 4332–4339. https://doi.org/10.1021/la062607k.
(15) Likos, C. N.; Vaynberg, K. A.; Löwen, H.; Wagner, N. J. Colloidal Stabilization by Adsorbed Gelatin. *Langmuir* **2000**, *16* (9), 4100–4108. https://doi.org/10.1021/la991142d.
(16) Lloyd, J. A.; Ng, S. H.; Davis, T. J.; Gómez, D. E.; Bach, U. Size Selective Adsorption of Gold Nanoparticles by Electrostatic Assembly. *J. Phys. Chem. C* **2017**, *121* (4), 2437–2443. https://doi.org/10.1021/acs.jpcc.6b10218.
(17) Bishop, K. J. M.; Grzybowski, B. A. "Nanoions": Fundamental Properties and Analytical Applications of Charged Nanoparticles. *ChemPhysChem* **2007**, *8* (15), 2171–2176. https://doi.org/10.1002/cphc.200700349.

Soft-computing based Technological Support for Droplet Epitaxially Grown Zero-dimensional GaAs Structures

Zoltán Farkas, Antal Ürmös and Ákos Nemcsics*

Institute of Microelectronics and Technology, Óbuda University,Tavaszmező utca 17. 1084 Budapest, Hungary

The research of 0D nanostructures is the part of current technological research. Recent and future applications of the nano-technology cover various devices, such as PV devices, LED's, lasers, and also devices for quantum computing.

The droplet-epitaxy is a novel technique for fabricating nano-structures on a semiconductor substrate. The droplet epitaxy is a part of the wider molecular beam epitaxal technology. The droplet-epitaxy is a technological tool for the preparation of various shaped nano-structures. According to a possible classification, these nano-strucures can be parted into three main types such as quantum-dots, quatum-rings and nano-holes. Where, so called inverted Quantum-dots are produced by filling nano-holes up. Our research concentrates on these structures.

There are several papers in the relevant literature that describe both the technology of fabrication and the geometry (e.g AFM scan) of the fabricated nano-structures. Thus a data-base have been created that includes all the three the surface density, the technological (growth temperature, annealin, Arsenic pressure, molecular flux etc.) and geometrical parameters (high, diameter, size of the deepness etc.) of the nanostructures. In this paper, with the help of soft-computational support, the relation among the technological (6-dimensinal space) and geometrical (5-dimensional space) are researched.

.

Keywords: zero-dimension, droplet-epitaxy, soft-computing

References

[1] Ákos Nemcsics: Quantum Dots Prepared by Droplet Epitaxial Method; https://www.intechopen.com/chapters/48775
[2] Z. Farkas, A. Ürmös, Á. Nemcsics: Softcomputational support for Technology of Droplet Epitaxal Nano-structure Growth (under publication in IEE proc.)
[3] Z. Farkas, A. Ürmös, Á. Nemcsics: Results of Principal Component Analyses on a Database of Gallium Arsenide-based Zero Dimensional Nanostructures (under publication in IEE proc.)
[4] Z. Farkas, A. Ürmös, Á. Nemcsics: Results of Regressing 0D Nanostructure Geometric Features on Production Process Parameters (under publication in IEE proc.).

Surface-enhanced Kretschmann-Raether ellipsometry based on plasmonic, Bragg and waveguide structures

Benjamin Kalas[1], György Sáfrán[1], Miklós Serényi[1], Kárpát Ferencz[2,3], Miklós Fried[1,4], and Peter Petrik[1*]

[1]*Institute of Technical Physics and Materials Science, Centre for Energy Research, Konkoly-Thege Rd. 29-33, Budapest 1121, Hungary*

[2]*Institute for Solid State Physics and Optics, Wigner Research Centre for Physics, Konkoly-Thege Rd. 29-33, Budapest 1121, Hungary*

[3]*Optilab Ltd., Sulyok Str. 2, Budapest 1031, Hungary*

[4]*Institute of Microelectronics and Technology, Obuda University, Tavaszmezo Str. 17, Budapest 1084, Hungary*

**E-mail address: petrik.peter@ek-cer.hu*

Keywords: in-situ ellipsometry, plasmonics, Kretschmann-Raether configuration, Bragg multilayer, waveguide

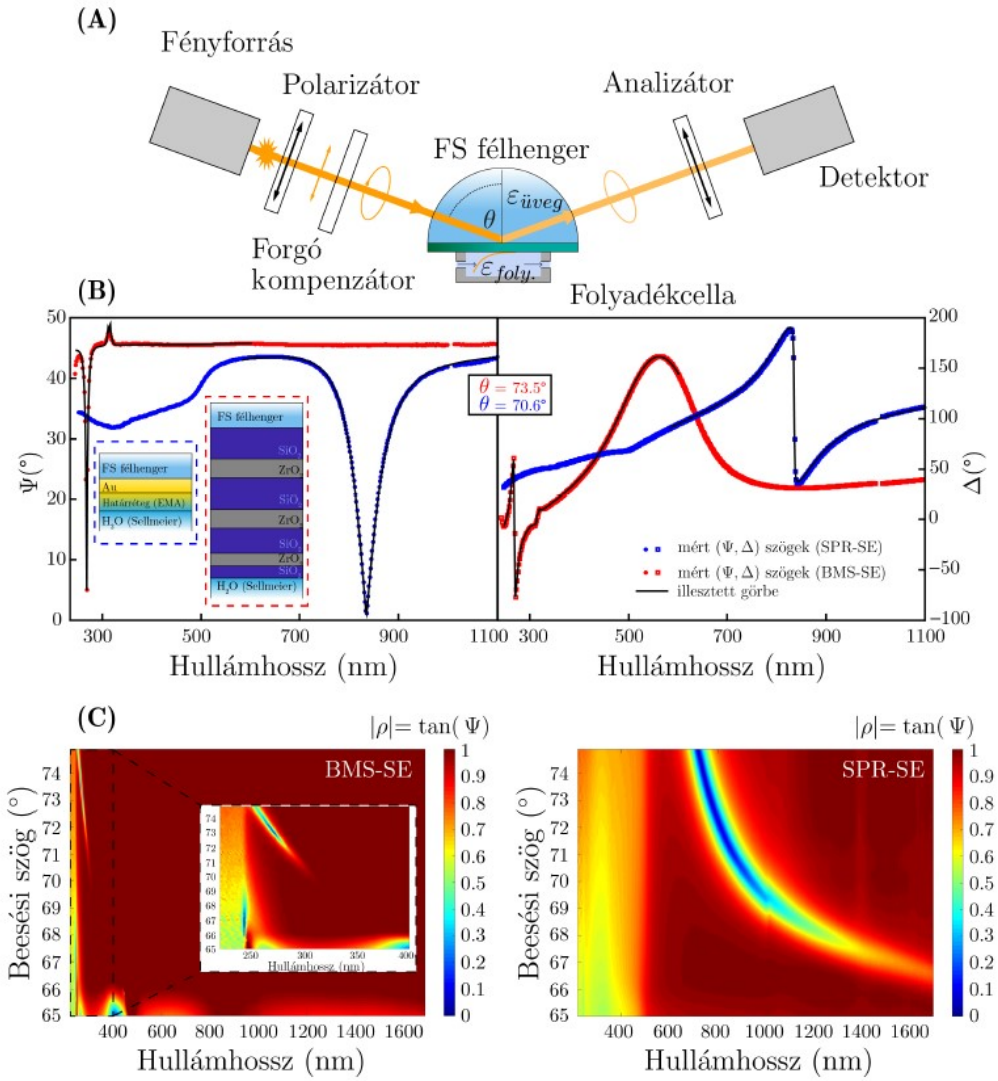

Figure 1 (A) Kretschmann-Raether ellipsometry configuration (B) Spectroscopic Ellipsometry spectra for Surface Plasmon Resonance (SPR, blue curves) and Bragg multilayer create resonant Bloch surface wave structures (BMS, red curves) (C) sensitivity maps in the Angle-of-Incidence - Wavelength graph for BMS-SE (left) and SPR-SE (right)

The advantage of Kretschmann-Raether ellipsometry has been demonstrated in numerous articles [1, 2, 3], in the first applications mainly focusing on plasmonics by a gold layer [3, 4]. In this case the resonant wavelength is inherent with the dielectric properties of gold, and therefore cannot easily be adapted to specific problems [5]. Furthermore, the spectral absorption peak is relatively broad compared with resonant multilayer structures. It has recently been shown that Bragg multilayers can be used to create resonant Bloch surface wave structures at arbitrary absorption peaks adapted to the investigated material, which has been demonstrated on the example of the 280-nm absorption of fibrinogen [6]. (See, Fig. 1) In this study we show that Bragg/hybrid plasmonic-Bragg structures and compositional grading of plasmonic metals (ultrathin combinatorial Ag_xAl_{1-x} layer) combined with waveguide layers can provide multiple spectral positions of the resonance in a wide wavelength range from the UV to NIR by using phase-sensitive Kretschmann-Raether ellipsometry. We show that both the spectral position and the polarization of the absorption peaks can easily be manipulated by using these nanostructures. (See Fig. 2!) Our results are supported by numerical calculations (transfer matrix and finite element methods) and experimental investigations as well.

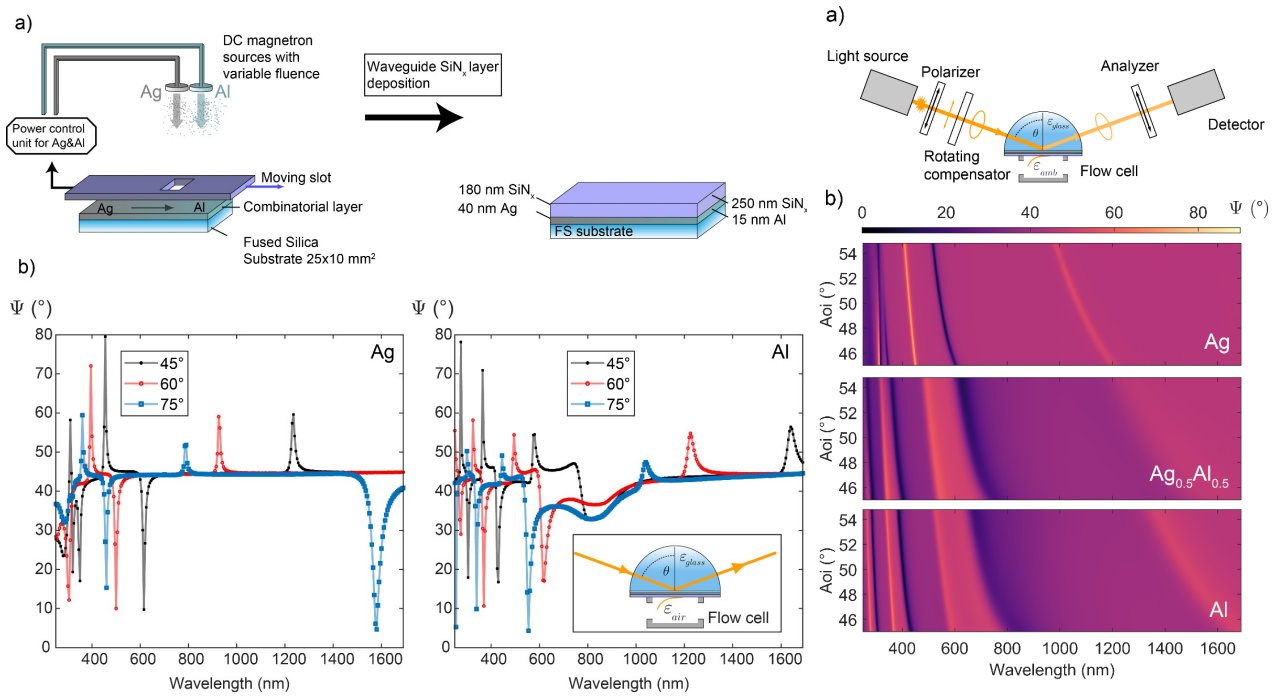

Fig. 2 Compositional grading of plasmonic ultrathin combinatorial Ag_xAl_{1-x} layer combined with waveguide layer can provide multiple spectral positions of the resonance in a wide wavelength range from the UV to NIR by using phase-sensitive Kretschmann-Raether ellipsometry. Left a) shows the preparation method b) shows example spectra at different angle-of-incidences with tunable resonance peaks. Right a) shows the measuring configuration b) shows the resonance peak position at different compositions.

References

[1] Abelès, F. Surface electromagnetic waves ellipsometry. Surface Science 56 (1976) 237–251.

[2] Bortchagovsky, E. G. Possibilities of ellipsometry with surface plasmon excitation in the investigation of thin films in comparison to separated ellipsometry and surface plasmon spectroscopy. in SPIE PRoc. 3094 (1997) 239–249.

[3] Poksinski, M. & Arwin, H. Protein monolayers monitored by internal reflection ellipsometry. Thin Solid Films 455–456 (2004) 716–721.

[4] J. Nador, B. Kalas, A. Saftics, E. Agocs, P. Kozma, L. Korosi, I. Szekacs, M. Fried, R. Horvath, P. Petrik, Plasmon-enhanced two-channel in situ Kretschmann ellipsometry of protein adsorption, cellular adhesion and polyelectrolyte deposition on titania nanostructures, Opt. Express. 24 (2016) 4812.

[5] B. Kalas, J. Nador, E. Agocs, A. Saftics, S. Kurunczi, M. Fried, P. Petrik, Protein adsorption monitored by plasmon-enhanced semi-cylindrical Kretschmann ellipsometry, Applied Surface Science. 421 (2017) 585–592.

[6] B. Kalas, K. Ferencz, A. Saftics, Z. Czigany, M. Fried, P. Petrik, Bloch surface waves biosensing in the ultraviolet wavelength range – Bragg structure design for investigating protein adsorption by in situ Kretschmann-Raether ellipsometry, Applied Surface Science. 536 (2021) 147869.

Nanoparticle gel networks as a novel platform in electrochemical sensing

Dániel Zámbó[1,2*]

[1]*Institute of Physical Chemistry and Electrochemistry, Leibniz Universität Hannover, Hanover 30167, Germany (*daniel.zambo@pci.uni-hannover.de)*
[2]*Institute of Technical Physics and Materials Science, Centre for Energy Research, Budapest 1121, Hungary (*daniel.zambo@ek-cer.hu)*

Nanoparticle gel networks represent a novel class of materials, in which the nanoscopic properties of the building blocks can be retained or even extended in the form of macroscopic gel structures. Among the modern nanocrystal gels, chemical, physical gels and cryogelated structures are promising candidates as sensors, photo(electro)catalysts and solar energy harvesters. Up to now, plasmonic noble metal nanorods (NRs) have been underrepresented as building blocks of the gelated macrostructures partly due to their relatively large sizes and the lack of reliable synthesis routes, which could provide nanorod solutions in high particle concentrations. In this paper, we demonstrate that by overcoming the above-mentioned limitations gold and silver nanorod cryoaerogel electrodes can be prepared. These porous nanostructured gel networks are of great interest in electrochemical sensing, ethanol oxidation reaction as well as in glucose sensing.

Keywords: nanoparticle gels, semiconductor/hybrid/composite nanoparticles, assembly, electrochemical sensing

Introduction

Nanocrystal aerogels are self-supported, porous, macroscopic particle networks consisting of interconnected nanoparticles (NPs).[1] The fabrication of these gel structures starts with the preparation of a highly concentrated (but colloidally stable) nanoparticle solution. The interparticle interactions between the NPs are manipulated via an external trigger to destabilize the solution and initiate the formation of a viscous colloid and later a solvogel network.[2] Based on the trigger we apply, two types of NP gels can be distungushed: the chemical and physical gels. Whilst in the chemical gelation, mostly an oxidative[3–8] or ionic trigger[2,9,10] is used to initiate the gelation, physical gels are prepared via applying phyiscal forces such as e.g. freezing.[11–13] Chemical gels are usually dried supercritically (to form aerogels)[2] or in controlled ambient conditions (to form xerogels)[9,14], cryoaerogels are fabricated via lyophyilization of the gel structure (Figure 1).[11,15,16]

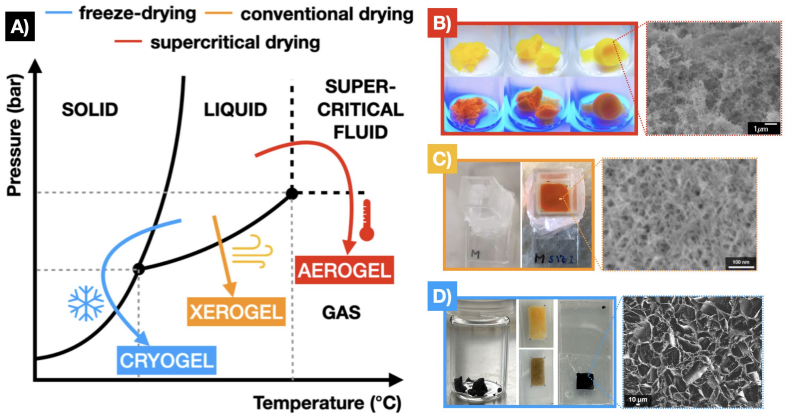

Figure 1. Types of drying methods (A). CdSe/CdS nanorod gel network prepared by chemical gelation (B) and xerogelation (C). Cryogelated structures built up from noble metal and semiconductor nanoparticles (D).

The cryoaerogelation is a novel process to assemble the nanoscopic building blocks into gel networks with open porosity and various macrostructural appearance. Figure 2 demonstrates the steps of the process starting with the filling of a pre-fabricated mold with the concentrated NP solution, followed by a flash-freezing (at 113 K) and a freeze drying step to prepare and remove the ice crystal template, respectively. As

a result, the nanoparticles are confined into the boundaries of the forming ice crystals manifesting itself as nanostructured sheets standing mainly perpendicular to the substrate.[11,12]

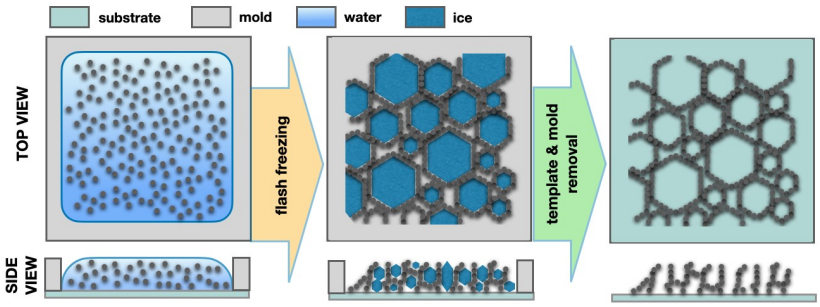

Figure 2. Schematic steps of the cryoaerogelation process: filling the mold with the concentrated NP solution, flash-freezing to trigger the rapid formation of the ice crystals, and the removal of the ice template via lyophilization to prepare a dendritic open pore structure.

Results and discussion

Nanocrystal cryoaerogels were prepared from the colloidal solution of AgNRs and AuNRs.[11] The noble metal nanorods were prepared by the seeded-growth method[17–19] (Figure 3A,B) and were upscaled to reach the desire concentration for cryogelation (ca. 5-8 g/L). The ensure the stability as well as to enhance the conductivity of the nanoparticles, the surface of the NRs were modified with a conductive polymer (PEDOT:PSS).[11]

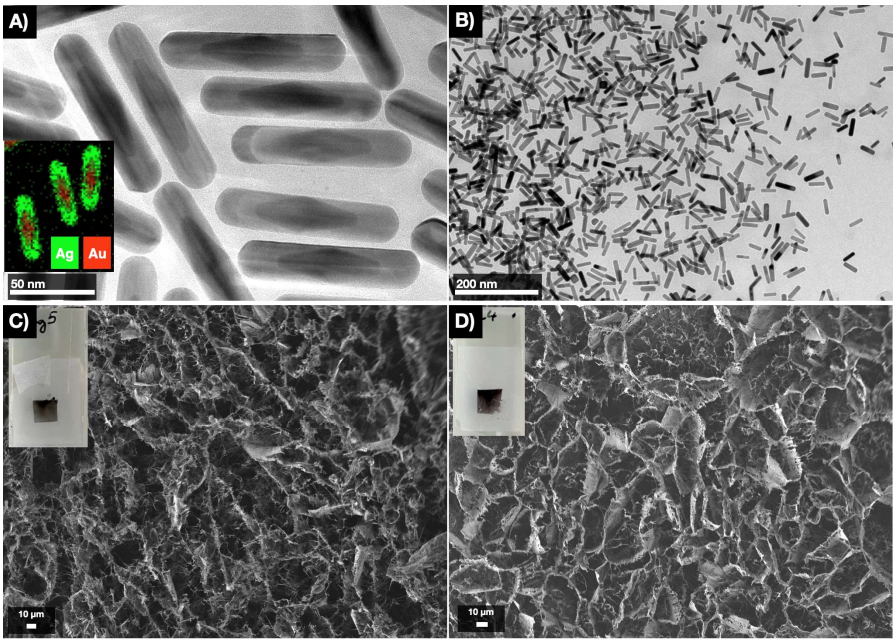

Figure 3. TEM and SEM images of the nanoparticle building blocks and their cryoaerogel structures: colloidal (A) and cryoaerogelated (C) AgNRs, colloidal (B) and cryogelated (D) AuNRs.

The NR cryoaerogels were fabricated on conductive ITO-covered glass slides, which were previously modified with MPTMS linkers to faciliate the attachment of the NRs to the substrate.[11] Figure 3C,D show the microstructure of the cryoaerogel coatings (as well as their physical appearance in the insets): the gel structures have a dendritic open-pore system with macropores (connected standing sheets) as well as mesopores (within the sheets). The sheets consist of the NRs, which preserves their original morphology.

This fabrication method enhances the specific surface area and increase the availability of the electrocatalytically active surface sites of the noble metal NRs.

The cryoaerogel electrodes were tested in different electrochemical/electrocatalytical model reactions.[11] Compared to the MPTMS-coated ITO electrodes, gold NR cryoaerogel-electrode showed enhanced activity in the redox transition of $K_4Fe(CN)_6/K_3Fe(CN)_6$ pair (in 1mM, Figure 4A), in ethanol oxidation reaction (in 1M EtOH concentration, EOR) at alkaline pH (Figure 4B) as well as in the electrochemical sensing of glucose (100 mM) at alkaline pH (Figure 4C). These test reactions demonstrate, that the NRs in the cryoaerogel structures retain their electrochemically active surface sites in spite of the presence of the polymer coating. Additionally, the polymer coating faciliates the charge transport within the gel structure and enhances its overall conductivity.[11]

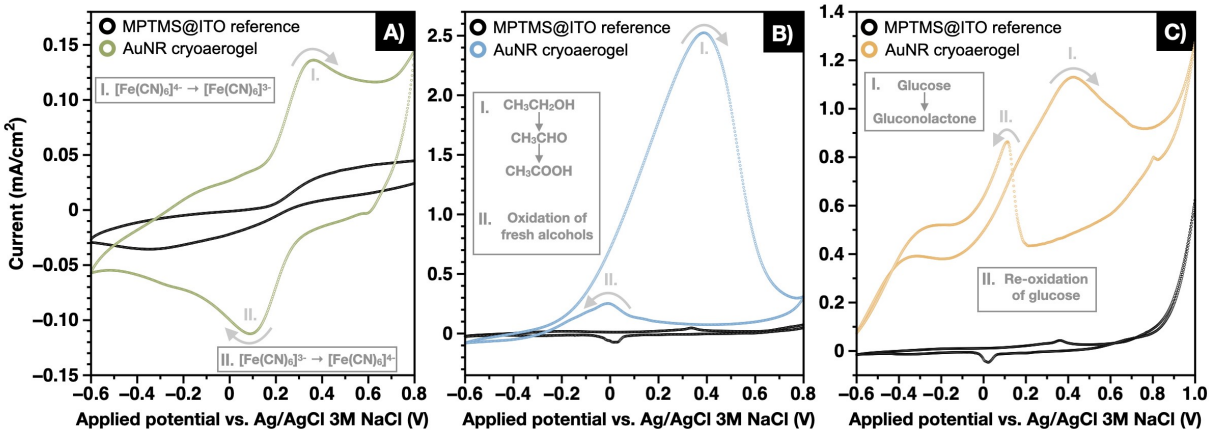

Figure 4. Electrocatalytic response of AuNR cryoaerogels in redox sensing (A), ethanol oxidation reaction (B) and glucose sensing (C). The corresponding Roman numbers represents the chemical redox processes taking place during the anodic and cathodic scans.

Conclusion and outlook

AgNRs and AuNRs were used as building blocks for the fabrication of novel, porous electrode materials. Cryoaerogelation is a promising technique for the preparation of nanoparticle-based macroscopic gel structures with tunable nanoscopic properties, micro- and macrostructure as well as macroscopic shapes (monoliths, coatings). *Via* controlling the surface chemistry of the building blocks, properties can be controlled at the nanoscale opening up new routes towards the fabrication of unique assembled structures from vast of different nanoparticles with different size, shape, compisiton, surface ligands and in various combinations.

References

(1) Rusch, P.; Zámbó, D.; Bigall, N. C. Control over Structure and Properties in Nanocrystal Aerogels at the Nano-, Micro-, and Macroscale. *Acc. Chem. Res.* **2020**, 53 (10), 2414–2424. https://doi.org/10.1021/acs.accounts.0c00463.

(2) Zámbó, D.; Schlosser, A.; Rusch, P.; Lübkemann, F.; Koch, J.; Pfnür, H.; Bigall, N. C. A Versatile Route to Assemble Semiconductor Nanoparticles into Functional Aerogels by Means of Trivalent Cations. *Small* **2020**, 16 (16), 1906934. https://doi.org/10.1002/smll.201906934.

(3) Sanchez-Paradinas, S.; Dorfs, D.; Friebe, S.; Freytag, A.; Wolf, A.; Bigall, N. C. Aerogels from CdSe/CdS Nanorods with Ultra-Long Exciton Lifetimes and High Fluorescence Quantum Yields. *Adv. Mater.* **2015**, 27 (40), 6152–6156. https://doi.org/10.1002/adma.201502078.

(4) Naskar, S.; Miethe, J. F.; Sánchez-Paradinas, S.; Schmidt, N.; Kanthasamy, K.; Behrens, P.; Pfnür, H.; Bigall, N. C. Photoluminescent Aerogels from Quantum Wells. *Chem. Mater.* **2016**, 28 (7), 2089–2099. https://doi.org/10.1021/acs.chemmater.5b04872.

(5) Naskar, S.; Freytag, A.; Deutsch, J.; Wendt, N.; Behrens, P.; Köckritz, A.; Bigall, N. C. Porous Aerogels from Shape-Controlled Metal Nanoparticles Directly from Nonpolar Colloidal Solution. *Chem. Mater.* **2017**, 29 (21), 9208–9217. https://doi.org/10.1021/acs.chemmater.7b03088.

(6) Rosebrock, M.; Zámbó, D.; Rusch, P.; Pluta, D.; Steinbach, F.; Bessel, P.; Schlosser, A.; Feldhoff, A.; Hindricks, K. D. J.; Behrens, P.; Dorfs, D.; Bigall, N. C. Spatial Extent of Fluorescence Quenching in Mixed Semiconductor–Metal Nanoparticle Gel Networks. *Adv. Funct. Mater.* **2021**, 31 (41), 2101628. https://doi.org/10.1002/adfm.202101628.

(7) Rusch, P.; Schremmer, B.; Strelow, C.; Mews, A.; Dorfs, D.; Bigall, N. C. Nanocrystal Aerogels with Coupled or Decoupled Building Blocks. *J. Phys. Chem. Lett.* **2019**, 10 (24), 7804–7810. https://doi.org/10.1021/acs.jpclett.9b02695.

(8) Rusch, P.; Niemeyer, F.; Pluta, D.; Schremmer, B.; Lübkemann, F.; Rosebrock, M.; Schäfer, M.; Jahns, M.; Behrens, P.; Bigall, N. C. Versatile Route to Core-Shell Reinforced Network Nanostructures. *Nanoscale* **2019**, 11 (32), 15270–15278. https://doi.org/10.1039/c9nr03645h.

(9) Zámbó, D.; Schlosser, A.; Graf, R. T.; Rusch, P.; Kißling, P. A.; Feldhoff, A.; Bigall, N. C. One-Step Formation of Hybrid Nanocrystal Gels: Deposition of Metal Domains on CdSe/CdS Nanorod and Nanoplatelet Networks. *Adv. Optical Mater.* **2021**, 9 (17), 2100291. https://doi.org/10.1002/adom.202100291.

(10) Schlenkrich, J.; Zámbó, D.; Schlosser, A.; Rusch, P.; Bigall, N. C. Revealing the Effect of Nanoscopic Design on the Charge Carrier Separation Processes in Semiconductor-Metal Nanoparticle Gel Networks. *Adv. Optical Mater.* **2021**, 2101712. https://doi.org/10.1002/adom.202101712.

(11) Zámbó, D.; Rusch, P.; Lübkemann, F.; Bigall, N. C. Noble Metal Nanorod Cryoaerogels with Electrocatalytically Active Surface Sites. *ACS Appl. Mater. Interfaces* **2021**, acsami.1c16424. https://doi.org/10.1021/acsami.1c16424.

(12) Müller, D.; Zámbó, D.; Dorfs, D.; Bigall, N. C. Cryoaerogels and Cryohydrogels as Efficient Electrocatalysts. *Small* **2021**, 17 (18), 2007908. https://doi.org/10.1002/smll.202007908.

(13) Müller, D.; Klepzig, L. F.; Schlosser, A.; Dorfs, D.; Bigall, N. C. Structural Diversity in Cryoaerogel Synthesis. *Langmuir* **2021**, 37 (17), 5109–5117. https://doi.org/10.1021/acs.langmuir.0c03619.

(14) Lübkemann, F.; Miethe, J. F.; Steinbach, F.; Rusch, P.; Schlosser, A.; Zámbó, D.; Heinemeyer, T.; Natke, D.; Zok, D.; Dorfs, D.; Bigall, N. C. Patterning of Nanoparticle-Based Aerogels and Xerogels by Inkjet Printing. *Small* **2019**, 15 (39), 1902186. https://doi.org/10.1002/smll.201902186.

(15) Freytag, A.; Sánchez-Paradinas, S.; Naskar, S.; Wendt, N.; Colombo, M.; Pugliese, G.; Poppe, J.; Demirci, C.; Kretschmer, I.; Bahnemann, D. W.; Behrens, P.; Bigall, N. C. Versatile Aerogel Fabrication by Freezing and Subsequent Freeze-Drying of Colloidal Nanoparticle Solutions. *Angew. Chem. Int. Ed.* **2016**, 55 (3), 1200–1203. https://doi.org/10.1002/anie.201508972.

(16) Freytag, A.; Günnemann, C.; Naskar, S.; Hamid, S.; Lübkemann, F.; Bahnemann, D.; Bigall, N. C. Tailoring Composition and Material Distribution in Multicomponent Cryoaerogels for Application in Photocatalysis. *ACS Appl. Nano Mater.* **2018**, 1 (11), 6123–6130. https://doi.org/10.1021/acsanm.8b01333.

(17) González-Rubio, G.; Kumar, V.; Llombart, P.; Díaz-Núñez, P.; Bladt, E.; Altantzis, T.; Bals, S.; Peña-Rodríguez, O.; Noya, E. G.; MacDowell, L. G.; Guerrero-Martínez, A.; Liz-Marzán, L. M. Disconnecting Symmetry Breaking from Seeded Growth for the Reproducible Synthesis of High

Quality Gold Nanorods. *ACS Nano* **2019**, 13 (4), 4424–4435. https://doi.org/10.1021/acsnano.8b09658.

(18) Sánchez-Iglesias, A.; Zhuo, X.; Albrecht, W.; Bals, S.; Liz-Marzán, L. M. Tuning Size and Seed Position in Small Silver Nanorods. *ACS Mater. Lett.* **2020**, 1246–1250. https://doi.org/10.1021/acsmaterialslett.0c00388.

(19) Li, X.; Lyu, J.; Goldmann, C.; Kociak, M.; Constantin, D.; Hamon, C. Plasmonic Oligomers with Tunable Conductive Nanojunctions. *J. Phys. Chem. Lett.* **2019**, 10 (22), 7093–7099. https://doi.org/10.1021/acs.jpclett.9b03185.

Analysis of the microstructure of color etched low carbon steel with spectroscopic ellipsometry

József Bálint Renkó [1*], Alekszej Romanenko [2,3], Péter János Szabó [1], Péter Petrik [2], Attila Bonyár [4]

[1]*Department of Materials Science and Engineering, Faculty of Mechanical Engineering Budapest University of Technology and Economics, Budapest, Hungary.*
[2]*Centre for Energy Research, Institute of Technical Physics and Materials Science, Budapest, Hungary*
[3]*Doctoral School of Chemistry, Eötvös Loránd University, Budapest, Hungary*
[4]*Department of Electronics Technology, Faculty of Electrical Engineering and Informatics, Budapest University of Technology and Economics, Budapest, Hungary*

The purpose of color etching as a preparatory process is to make the microstructure visible for metallographic evaluations. However, the layer formed during the etching process carries significantly more information inside. It allows us to deduce not only the chemical composition of the present phases, but also the orientation of the individual particles. Our work aims to explore these properties and expand the application areas of color etching. The layer formed during etching is examined by various methods. By comparing optical microscopy, backscattered electron diffraction, and spectroscopic ellipsometry, conclusions about the relationship between the formed layer and the orientation of each grain can be drawn.

Keywords: color etching, spectroscopic ellipsometry, EBSD, optical microscopy, analysis, material science

1. Introduction

Etching methods are very popular and frequently used in metallography [1-2]. They offer a quick and easy solution for developing the grain structure of different polished samples. The etchant reacts with the surface of the sample to change its topography, thus making the individual grains and grain boundaries visible. Although there are not many differences in the field of application of the different process variants, they can be divided into two main groups according to their mechanism of action.

The first group includes chemical etchants with a typically acidic pH. These react with the surface of the sample to dissolve the substrate into the solution. The development, i.e., the visualization of the microstructure, is thus caused by the difference in the rate of etching of the individual particles and the grain boundaries [3,4]. The process usually takes a few seconds but up to a maximum of a few minutes.

The second group includes the color etchants [5]. In terms of their prevalence, these are also commonly used developer processes, but they are being used significantly less than chemical etchants. This is due to the nature of the salt solutions used in color etching. On the one hand, there are fewer types available, and on the other hand, they are less aggressive, thus it takes much longer to achieve the proper effect. Color etching usually takes a minimum of a few minutes. During the process, the typically used metal salt solution reacts with the surface of the sample to form a thin, transparent film. The layer grows in both directions relative to the original plane of the sample as more and more material dissolves from the sample and the etchant. As the film grows, the color of each particle undergoes a cyclic color change that meets the interference criterion [6].

Although various etching processes have been widely used, the knowledge of the chemical processes is mostly unexplored. Studies to understand the etching phenomenon represent a relatively new direction in materials science, most of which can be traced back to the past decade. [7] [8-9]. The idea of an existing connection between crystallographic orientation and the color resulting from color etching can be traced back to 2010 [10-11].

In order to determine orientation by color etching, we developed a complex measurement and evaluation method in 2019, in which the grain orientation can be determined directly from color etching. The developed model made it possible to calculate the average etching rates for each grain and then assign them to the

appropriate orientations. Using the model, the angles of the surface of each particle with the main crystallographic orientations [100] and [111] in a randomly selected area were determined using optical microscopy only with an average absolute error of 3-5° compared to the electron backscatter diffraction (EBSD) measurements [12].

In our work, we sought the answer to whether spectroscopic ellipsometry is suitable for examining the layer formed during etching and whether the measurement can confirm the results of the previously developed methodology with it.

2. Experimental

2.1. Materials and methods

Spheroidal graphite cast iron was used as a sample to develop the original methodology [12]. Due to the graphite's microstructure, the same area could be easily identified multiple times. Beraha I solution was chosen as an etchant, which can be prepared by dissolving 3 g $K_2S_2O_5$ and 10 g $Na_2S_2O_3$ in 100 ml of distilled water. Beraha I interacts with the ferrite phase, making it an excellent tool for examining low carbon steel and cast iron samples [13].

Unfortunately, the smallest area that can be scanned by the spectroscopic ellipsometer at the settings to be used has a diameter of approx. 0.2 mm, which is not possible in the case of cast iron, as the grain size of the tested cast iron was about an order of magnitude smaller. Modifying the sample was necessary to allow direct measurement of each particle with ellipsometry. In order to be able to continue the experiment without changing the etchant, DC01 low-carbon ferritic steel was chosen as a new sample.

To achieve the required grain size, the DC01 sample was heated to 850 °C and allowed to cool slowly to maximize grain coarsening [14]. As a result, 1-3 mm particles were formed. Further studies were performed in air-conditioned laboratories, the temperature was set to 21 °C everywhere.

2.2. Instrumentation

Spectroscopic ellipsometry illuminates the surface of the sample with a light beam of known polarization and measures the change in polarization during reflection. The method can determine the phase difference between the two polarization directions. That makes it is much more sensitive than conventional reflectometry, so a resolution of up to 0.1 nm can be achieved. The optical density (refractive index) can also be determined with a resolution of 0.001 [15].

The measurement can be performed at a point in up to a few seconds over a wide spectral range, allowing the modeling of complex layer structures and the determination of their parameters. Due to the fast measurement, it is also possible to map larger surfaces in real-time. The samples were placed on a workbench of a Woollam M-2000 DI rotary compensating spectroscopic ellipsometer with a wavelength range from 190 nm to 1690 nm. The measurements lasted a total of 2×16 s at each point, with a step size of 175 µm. The spot elongated in the direction of the plane of incidence due to the used large angle of incidence (70 °).

Ellipsometry is a highly surface-sensitive method. Thus, proper consideration of the surface is paramount to determine the bulk refractive index of materials. Unfortunately, in this case, it is not possible to assume that the refractive index of the substrate is the same and only the thickness of the surface layer is different. Grains oriented in different directions have different optical properties. We created an optical model in which the steel sample was described with Lorentz oscillators at each measurement point. The wavelength dependence of the refractive index of the surface layer was characterized by a simple Cauchy dispersion [16,17].

To record the images of color etching, a DP72 digital camera connected to an Olympus BX51 optical microscope was used.

EBSD examinations were performed with a TSL-EDAX EBSD system connected to a Philips XL-30 scanning electron microscope. The slight distortion seen in the pole figures is due to the uncertainties of tilted image recording at a tilt angle of 70 ° and the correction software.

3. Results and discussion

After etching, 30 grains were selected on the examined surface, all of which were clearly identifiable on the surface maps of EBSD and ellipsometry as well (Fig. 1). Comparing the three images, the surface layer of up to a few hundred nanometers formed on each particle makes each grain well identifiable. The layer thickness and grain orientation of particles of similar color are nearly the same. An example of this is the comparison of particles 1 and 3, or 12 and 23. The visual data confirm our previous hypothesis about the connection between the etching rate and grain orientation [12].

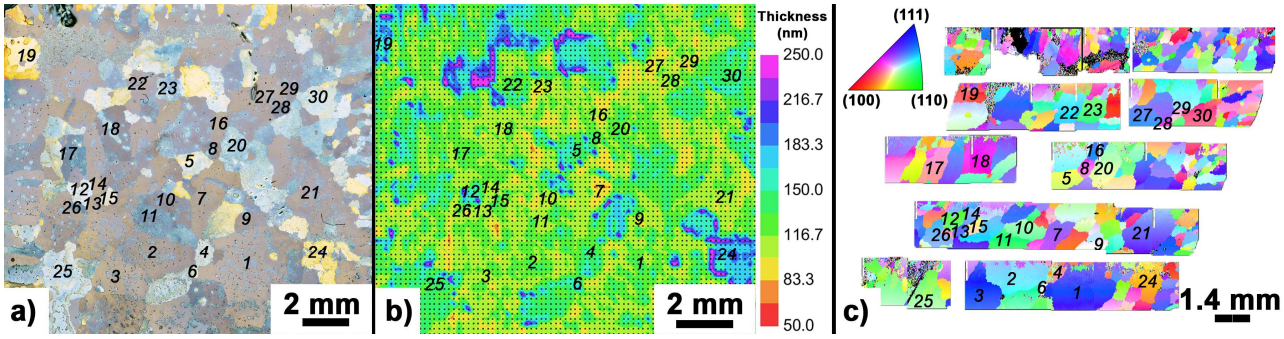

Fig. 1. Optical microscopic image of the selected area on the color etched surface (a), layer thickness map determined by spectroscopic ellipsometry (b), and inverse pole figure determined by EBSD (c)

Based on the model assuming a homogeneous layer fitted to the ellipsometry results, the refractive index and thickness of the layer at each measurement point were determined (Fig. 2). Since the size of the smallest area that can be scanned by ellipsometry is given, the individual grain boundaries can only be clearly identified if the particles are significantly larger than this.

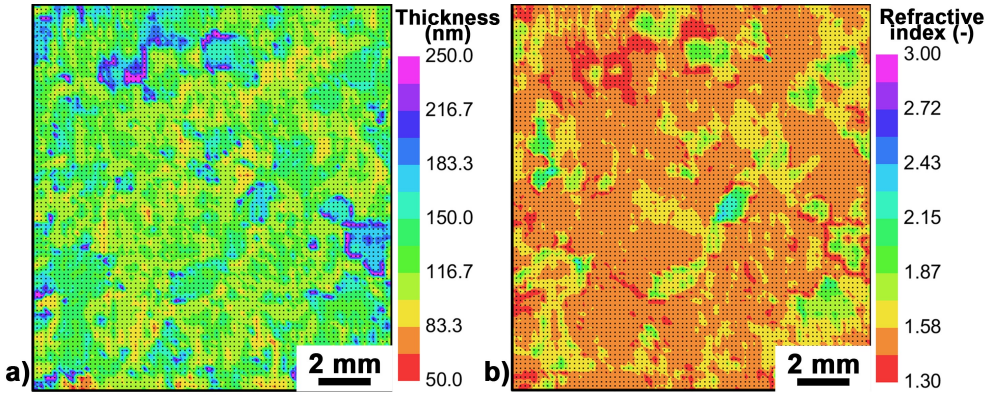

Fig. 2. Layer thickness (a) and refractive index (b) maps measured by spectroscopic ellipsometry

As published in 2019, the normalized color intensity measured during color etching was of a decaying cosine nature for each grain. Comparing the intensity curves of the particles with different orientations, the difference was given by the time required to reach each extreme value. Grains whose orientation was at a smaller angle to the direction [100] etched faster, thus, they reached individual extremes earlier [12].

For the light components of different wavelengths (in this study, the colors red, green, and blue), the correlation between the time required to reach the first minimum on the cast iron sample and the angle enclosed in the principal crystallographic directions is shown in Fig. 3.a. The strong positive correlation for the direction [100] suggests that the smaller the closed angle between the [100] and the surface normal of the investigated particle, the less time it takes to reach the first minimum on the intensity curves, and consequently the faster the grain is etched.

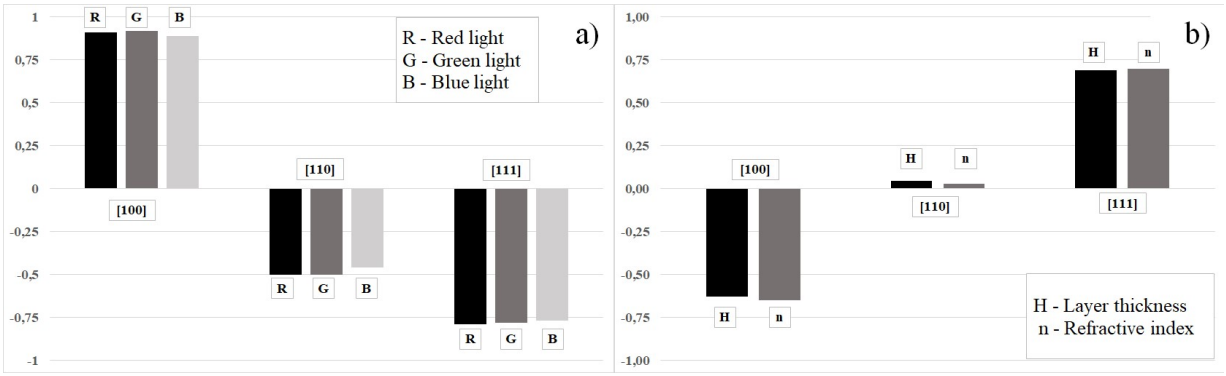

Fig. 3. The correlation for cast iron between the time required to achieve the same layer thickness and the angle of the grain orientation with the main crystallographic directions using different color components (a) and the correlation for ferritic steel between the grain orientation and the refractive index as well as the layer thickness (b)

To quantify the visual results of ellipsometry on ferritic steel, we examined the correlation between the angle enclosed with the main crystallographic directions and the layer thickness and refractive index for the selected grains (Fig. 3b). The correlation between the angle enclosed with [100] and [111] and the refractive index and the closely related layer thickness was almost the same as in the previous studies. The inverse nature can be explained by the larger the angle with the given main direction, the slower the etching, and consequently, the smaller the thickness of the formed layer. This, in turn, reaffirms the results of previous measurements and studies.

4. Summary

The refractive index and the thickness of the layer formed during color etching were measured by spectroscopic ellipsometry, expanding the range of suitable equipment with a new device. The results of the measurement are in line with previous results. The crystal orientation-dependent etching speed correlates mostly with the angle enclosed with [100]. The smaller the enclosed angle with it, the faster the etching proceeds and the thicker the emerging layer. Measurement by ellipsometry also confirmed a smaller but inverse correlation with [111] and a lack of correlation with [110].

Acknowledgment

Supported by the ÚNKP-21-3-II-259 New National Excellence Program of the Ministry for Innovation and Technology from the source of the National Research, Development and Innovation Found

References

[1] G. Petzow: Metallographic Etching, 2nd Edition: Techniques for Metallography, Ceramography, Plastography, ASM International, 1999, ISBN 1615032207, 9781615032204, 1-240
[2] E. Beraha: Ätzmittel zur Sichtbarmachung chemischer und physikalischer Inhomogenitäten in Stahlgefügen, Prakt. Metallogr., vol. 4, no. 8, 1967, 419–420
[3] E. Beraha: Ätzmittel zur Identifizierung von Sulfideinschlüssen in Eisen und Stahl und zur Unterscheidung von Phosphid und Zementit in Gußeisen, Prakt. Metallogr., vol. 6, no. 9, 1969, 565–568
[4] HD. Um, N. Kim, K. Lee, et al.: Versatile control of metal-assisted chemical etching for vertical silicon microwire arrays and their photovoltaic applications, Sci Rep 5, 2015, 11277
[5] E. Beraha: Farbätzung für Gußeisen, Stähle, Werkzeugstähle, Manganstähle und ferritische und martensitische rostfreie Stähle, Prakt. Metallogr., vol. 8, no. 9, 1971, 547–550

[6] S. Chen, M.-L. Giorgi, J.-B. Guillot, G. Geneste: Oxidation and diffusion processes at the Mn-doped Fe(100) and Fe(110) surfaces from first-principles, Applied Surface Science 258, 2012, 8613-8618
[7] Y.A., Bioud, A. Boucherif, A. Belarouci, et al.: Chemical Composition of Nanoporous Layer Formed by Electrochemical Etching of p-Type GaAs, Nanoscale Res Lett 11, 2016, 446
[8] D. Britz: Opening the door to fundamental understanding of structure and color metallography - a correlative microscopy study on steel, Microsc. Microanal., 834, 2014, 1431-9276 1435-8115 20
[9] D. Britz: Reproducible surface contrasting and orientation correlation of low-carbon steels by time-resolved Beraha color etching, Mater. Perform. Characterization 5 (5), 2016, 553–563
[10] P.J. Szabó, I. Kardos: Correlation between grain orientation and the shade of color etching, Mater. Charact. 61 (08), 2010, 814–817
[11] A. Bonyár, P. J. Szabo: Correlation between the Grain Orientation Dependence of Color Etching and Chemical Etching, microscopy, and microanalysis: the official journal of Microscopy Society of America, Microbeam Analysis Society, Microscopical Society of Canada. 18. 2012, 1-4.
[12] A. Bonyár, J. Renkó, D. Kovács, P. J. Szabó: Understanding the mechanism of Beraha-I type color etching: Determination of the orientation dependent etch rate, layer refractive index and a method for quantifying the angle between surface normal and the 〈100〉, 〈111〉 directions for individual grains, Mater. Char., Vol. 156, 2019, 109844
[13] E. Beraha: New metallographic reagents for stainless steel and heat-resisting alloys, J. Iron Steel Inst., vol. March, 1966, 248–251
[14] E. Kiss, J. Gulyás, et. al.: Képlékeny alakítás, Budapest, Tankönyvkiadó, 1987, 95-100
[15] T. Lohner, M. Serényi, P. Petrik: Characterization of sputtered aluminum oxide films using spectroscopic ellipsometry, Intern. J. of New Horizons in Phys., 2 (1), 2015, 1-4
[16] H. G. Tompkins, J. N. Hilfiker: Spectroscopic ellipsometry: Practical application to thin film characterization, Momentum Press, LLC, New York, 2016, 31-55
[17] H. Fujiwara: Spectroscopic Ellipsometry: Principles and Applications, John Wiley & Sons Ltd, Chichester, 2007, 81-120

In-situ ellipsometry on the oxidation of zirconium at medium temperatures

A. Romanenko [1,2], E. Agócs [1], Z. Hózer [1], P. Petrik [1] and M. Serényi [1]

[1]*Centre for Energy Research, Konkoly-Thege Rd. 29-33, 1121 Budapest, Hungary*

[2]*Doctoral School of Chemistry, Eötvös Loránd University, Pázmány Péter sétány 1/A,H-1117 Budapest, Hungary*

We report on the growth of ZrO_2 films upon the gradual thermal annealing of Zr in the temperature range of 500-700 K. The thickness of the oxide was monitored by in-situ spectroscopic ellipsometry (SE) with temporal and thickness resolutions of 1 second and 1 nanometer, respectively. It has been observed that the oxide growing process stops immediately when the temperature is reduced only by a few degrees and this phenomenon is well reproducible. To describe this, we set up a simple phenomenological model.

Keywords: energy, challenges, abstract, template

1. Introduction

Most studies deal with the initial [1] or final [2] stage of Zr oxidation. The initial stage of oxidation, starting from a pure crysallin surface, under highaltitude vacuum, examined by a combination of insitu specroscopic ellipsometry (SE) and X-ray photoelectron spectroscopy, wellcontrolled and understood process.

There were only a few studies, including our group [3], that dealt with the optical measurement of the thickness of the oxide, but mainly by ex-situ characterizations on thin films. Here, we use the capabilities of SE for in-situ characterization with thickness and time resolution in the range of nanometers and seconds, respectively. These properties allow the development and control of an oxidation model in the thickness range of a few hundred nanometers. Further knowledge of the oxidation process in this range is essential in many applications, including nuclear technology and microelectronics.

2. Experimental procedures

2.1. Materials

Zr plates in sizes of approximately 1 cm by 2 cm made of an E125 alloy (Nb content of 2.5%) have been prepared. The samples have been polished to have an oxide surface layer thickness of only 3 - 6 nm gained from the ellipsometry az the start of the measurement. Our aim was to prepare a good and reproducible surface of optical quality that allows to record the ellipsometric spectra without depolarization and that can well be described by a simple optical model.

2.2 Annealing

The Zr samples were annealed in an isolated quartz tube in given O2/Ar gas mixture shown in Fig. 1. In the series of experiment the oxygen concentration was varied between 0% and 20%. A heating ceramic plate is mounted in the tube so that the surface of the samples placed on the ceramic plate

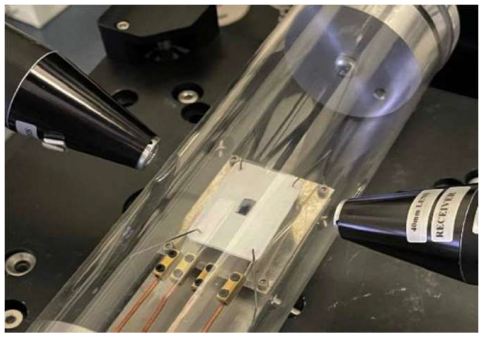

Fig. 1*. Heat cell constructed for multiple-angle ellipsometry measurements in controlled ambient and temperature.*

coincides with the axis of the tube. This configuration enables the ellipsometry measurement to be performed at any angles of incidence that is allowed by the equipment (in our case: 45° - 90°).

This setup makes even an automatic sample alignment possible due to that the aligment procedure can be performed also through the tube. The measurement beam was focused to make sure that the it enters the tube perpendicular to a surface over the whole spot which has a size of approximately 0.3 mm x 1.0 mm on the surface of the sample. The heating plate has a tolerance of up to 900 K. The accuracy of the temperature control is about 0.1 K. In these experiments, the temperature was increased at a rate of 10 K/min. After reaching a given tempreture – step the heat up was stupped until the oxide growth reached its saturation point. Immediately following that the temperature controller was turned of for 30 seconds to reduce the heat level, stopping the growth of the oxide layer immediately. The steps in the heating procеww were determined to be evenly distributed on the 1000/T scale . These steps were added to support our assumptions about the mechanics of layer growth. Thickness was determined in real time by ellipsometry during annealing to accurately control heat treatment times.

3. Discussion

3.1. Model of oxidation

The concept of the growth assumes the formation of dense oxide films on the metal surface by diffusion of oxygen anions through the oxide layer under the influence of a strong concentration gradient around the interface. All the free oxygen atoms migrate to the oxide-metal interface and react with the metal. However, because the anions move to the metal surface and take part in the reaction, they leave a positively charged region behind. This process continues until the region has a large enough electrical charge to repulse zirconium cations and prevent to enter the vicinity of the metal surface. Eventually, a tate of equilibrium will occur producing a “potential barrier" zone. If the region becomes completely depleted, and the oxidation process is stopped.

3.2. Analysis of the optical measurements

We apply the implified form of the Fick II. diffusion law to express the time dependence of the gradient of the O- anion flux:

$$J_d(x) - J = c_O \frac{dx}{dt} \qquad (1)$$

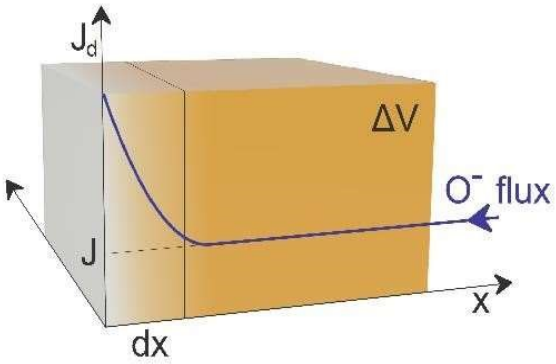

Fig. 2. *Schematic diagram of the kinetic model. The blue curve shows the anion flux (J_d) as a function of depth. The x = 0 position corresponds to the interface between the oxide and the substrate.*

where x and cO denotes the thickness of the oxide layer and the oxygen concentration, respectively (Fig. 2). Using the formalisms used in the physics of semiconductors, we can solve this differential equation and we obtain for the time dependence:

$$t = -\alpha x - \alpha\delta \cdot ln\left(1 - \frac{x}{\delta}\right), \qquad (2)$$

where δ and α denotes the final thickness of the oxide layer and the growth rate, respectively. A comparison of this equation and the measurements is shown in Fig. 3.

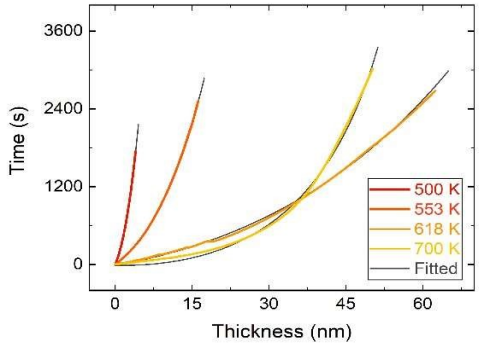

Fig. 3. *Time versus thickness (at 20% O2 concentration), determined from the optical model.*

4. Conclusions

A simple phenomenological model has been developed that attempts to compare the parameters of the transport properties of atomic oxygen (anions) with the kinetic results measured by the SE in the thickness range (from a few nanometers to a few hundred nanometers) that has not yet been studied in detail. We have shown that kinetic behavior can be described phenomenologically by the approach used to analyze p-n nodes in semiconductor physics.

Acknowledgements

Support from National Development Agency grants of OTKA K131515 and 2019-2.1.11-TET-201900004 is gratefully acknowledged.

References

[1]. A. Lyapin, L. P. H. Jeurgens, P. C. J. Graat, E. J. Mittemeijer, Ellipso-metric and XPS study of the initial oxidation of zirconium at room tem-perature, Surface and Interface Analysis (2004) 989–992.
[2]. H. I. Yoo, B. J. Koo, J. O. Hong, I. S. Hwang, Y. H. Jeong, A working hypothesis on oxidation kinetics of Zircaloy, Journal of Nuclear Materials 299 (2001) 235–241.
[3]. P. Petrik, A. Romanenko, B. Kalas, L. Péter, T. Novotny, E. Perez-Feró, B. Fodor, E. Agocs, Z. Hózer, Optical Properties of Oxidized, Hydrogenated and Native Zirconium Surfaces for Wavelengths from 0.3 to 25μm - A Study by Ex Situ and In Situ Spectroscopic Ellipsometry, Physica status solidi (a) (2019)1800676.

Microstructure of composition spread YTiO thin films

D. Olasz., V. Kis, P. Petrik, B. Kalas, G. Sáfrán

Materials with perovskite structure are receiving increasing attention in semiconductor research. They have a chemical formula ABX_3, where 'A' and 'B' are cations and X is an anion that bonds to both. A number of elements can be combined to form perovskite structure showing a wide variety of physical, optical, and electrical properties. Perovskite solar cells can be manufactured by simple, additive deposition techniques, like printing, for a fraction of the cost and energy compared to traditional silicon technology. Recently, the photoconversion efficiency of perovskite solar cells has exceeded 25%, close to that of silicon (27%) [REF]. From the large family of perovskites, we aimed to produce and characterize the Y-Ti-O system. Thin composition spread samples were deposited on carbon coated TEM grids by reactive DC magnetron sputtering of yttrium and titanium in $3 * 10^{-3}\ mbar$ Ar gas with $1 * 10^{-4}\ mbar$ O_2 inlet. Using microcombinatory [1], we could produce and examine the oxides of the cations in the whole Y_xTi_{1-x} (x=0…1) concentration range in a single sample (Figure 1).

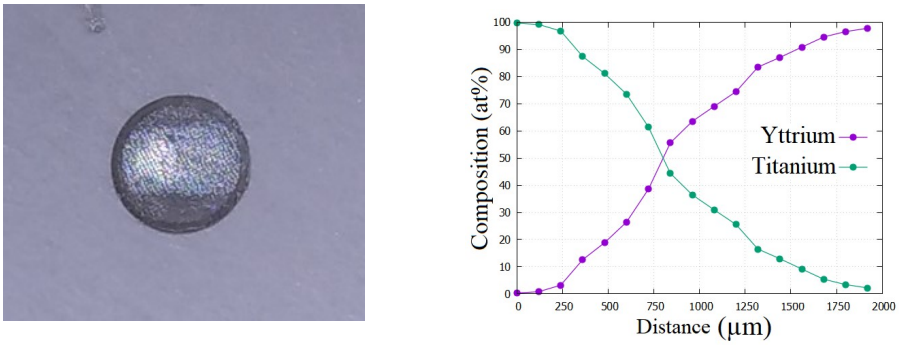

Figure 1: A combinatorial YTiO sample on a TEM grid and its EDS diagram representing concentration of the cations as a function of distance along the layer.

The microstructure as function of composition was determined by TEM and SAED: at high Y or Ti concentrations crystalline, while in between an amorphous structure was found (Fig.2).

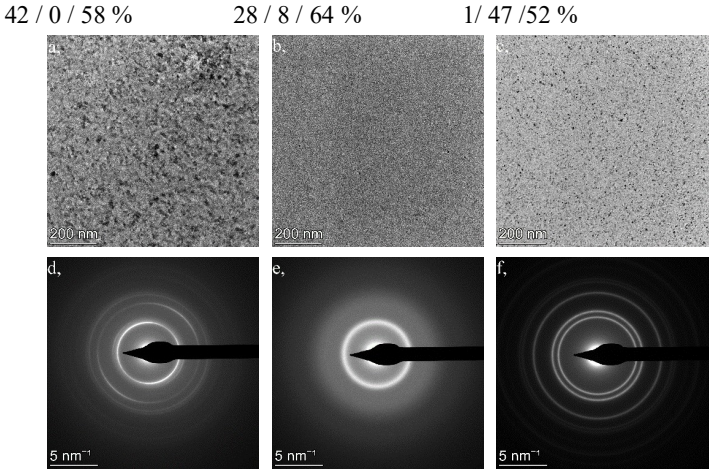

Figure 2. (a,b,c) BF TEM images of selected Y/Ti/O (at%) compositions **(d,e,f)** the corresponding SAED patterns. Sharp rings **(d, f)** show polycrystalline, while diffuse rings **(e)** represent amorphous structure.

Crystalline phases were determined by the evaluation of SAED measurements over the whole composition range with the help of the ProcessDiffraction software [2].

At the Ti surplus side of the sample, rocksalt-type cubic TiO structure (space group: $Fm\bar{3}m$, $a = 4.1766$ Å) was formed and the intensity of its characteristic peaks decreases with the increase of Y concentration. Between Y/Ti/O 14/28/58 and 28/8/64 at% compositions only diffuse peaks are present, characteristic for amorphous structure. With a further increase of the Y content, at 33/5/62 at% composition, the peaks of the Y_2O_3 crystalline phase appears, showing $Fm\bar{3}m$ space group, cubic ($a = 5.2644$ Å), CaF_2 type structure. At even higher Y concentration (33/5/62) additional small peaks appear representing a Mn_2O_3 bixbyite-type cubic structure of Y_2O_3 (space group: $Ia\bar{3}$, $a = 10.5981$ Å). It has a lattice constant twice as large as the one mentioned above, and its formation is related to the arrangement of O-vacancies.

To obtain perovskite structure, we will heat treat the samples. Data analysis is ongoing and publication of the results is planned.

Acknowledgements OTKA K 129009 is acknowledged.

References

[1] G. Sáfrán; Ultramicroscopy 187 (2018), 50-55

[2] J.L. Lábár; Microsc. Microanal. 14 (4) (2008), 287-295